International Journal of Solids and Structures 50 (2013) 297–309

Contents lists available at SciVerse ScienceDirect

International Journal of Solids and Structures

journal homepage: www.elsevier.com/locate/ijsolstr

Instrumented End Notched Flexure – Crack propagation and process zone monitoring. Part I: Modelling and analysis

J. Jumel [a,b,c,*], M.K. Budzik [a,b,c,d], N. Ben Salem [a,b,c,d], M.E.R. Shanahan [a,b,c]

[a] Univ. Bordeaux, I2M, UMR 5295, F-33400 Talence, France
[b] CNRS, I2M, UMR 5295, F-33400 Talence, France
[c] Arts et Metiers ParisTech, I2M, UMR 5295, F-33400 Talence, France
[d] French Space Agency (CNES) – DLA, 52 rue Jacques HILLAIRET, 75612 Paris Cédex, France

ARTICLE INFO

Article history:
Available online 24 September 2012

Keywords:
Bonded joints
End Notched Flexure
Mode II
Strain gauges

ABSTRACT

Analysis of the three-point bending, End Notched Flexure (ENF), test is presented for exploitation with a new experimental methodology using the backface strain monitoring technique. The model consists of two Timoshenko beams joined with a two parameter elastic foundation, to evaluate stress and strain fields in both adherends and the adhesive layer, together with the specimen compliance and energy release rate. This model is compared to a simplified case, from which a comprehensive experimental method is proposed for precise monitoring of crack propagation and measurement of interface shear compliance during the ENF experiment. In addition, simple formulae are proposed for evaluating mode II energy release rate, and possible experimental artefacts due to asymmetric loading conditions are evidenced.

1. Introduction

Adhesive bonding is becoming increasingly popular for joining materials and structures in many fields such as medicine (Duarte et al., 2011; Van Meerbeek et al., 1998), civil engineering (Oehlers, 2001), microelectronics (Li and Wong, 2006) and transport (Loven, 1999; Higgins, 2000). Contrary to mechanical fastening, this technique requires no drilling or machining of the parts, reduces stress concentrations and improves service lifetime. It also achieves secondary functions such as water and air tightness, vibration damping and many others.

However, structural joints often suffer from a lack of reliability due to somewhat empirical design methods. A large number of strength and toughness characterisation tests (Da Silva et al., 2009; He, 2011; Rodríguez et al., 2012), based on different specimen geometries, have shown different mechanical properties for essentially the same joint systems. To improve the characterisation and design of bonded joints, scientists have tried to refine analysis at the bondline scale to evaluate various intrinsic rather than geometry dependent properties (Cognard et al., 2006, 2011). At a mesoscale, cohesive zone models (CZM) are becoming very popular since they take into account complex force/displacement interface separation laws to model global behaviour of the assembly (Liljedahl et al., 2007). Nevertheless, these complex models suffer from insufficient experimental verification, the data showing poor sensitivity to the numerous parameters (Alfano, 2006; Gustafson and Waas, 2009). Besides, few methods are available for direct measurement of these cohesive laws (Sørensen and Jacobsen, 2009). Recently, we proposed to use backface strain monitoring instrumentation combined with double cantilever beam test specimens to investigate the cohesive force distribution in the bondline (Budzik et al., 2011a; Ben Salem et al., 2012). The experimental data reduction is based on the equivalent crack length concept (de Moura and de Morais, 2008; de Moura et al., 2006), combined with beams on elastic foundation models, to evaluate the extent of the process zone. This procedure has been applied to mode I and mixed mode II/III (Budzik et al., 2011b). However, bonded joints are generally loaded in shear, so that an extension of our instrumented crack propagation test protocol to mode II loading is required. We start with analysis of the three point bending End Notched Flexure (ENF) specimen, which is very popular for measuring the toughness of bonded joints or laminates in mode II. In this article, we concentrate on theoretical analysis of the experiment and propose a test protocol based on strain gauge instrumentation. In a second paper, the data reduction method is applied to analysis of crack propagation measurement in an aluminium specimen bonded with a structural epoxy adhesive.

The double cantilever beam (DCB) specimen is extensively used for bonded joint toughness measurement in mode I. On the contrary, there is no international consensus on mode II testing. Nevertheless, the three point bending test using the ENF configuration

* Corresponding author.
E-mail address: julien.jumel@u-bordeaux1.fr (J. Jumel).

0020-7683/$ - see front matter © 2012 Elsevier Ltd. All rights reserved.
http://dx.doi.org/10.1016/j.ijsolstr.2012.08.028

is probably the most popular, since both test set-up and specimen are simple. This test was introduced by (Barrett and Foschi, 1977) to study the fracture toughness of wood in shear. The simplest analytical expressions for mode II strain energy release rate, G_{II}, and specimen compliance were later developed by (Russel and Street, 1982), based on classic beam theory. As for DCB tests, numerous studies have been devoted to analysis, modelling and design of ENF specimens (Ding and Kortschot, 1999; Alfredsson, 2004; Carlsson et al., 1986; Chai and Mall, 1988; Corleto and Hogan, 1995; Ouyang and Li, 2009; Yang et al., 2001; Yoshihara, 2005; Qiao and Wang, 2005; Wang and Qiao, 2005). The main objectives concerned evaluation of the effects of experimental conditions (set-up, specimen geometry...) and of adherend and adhesive properties on specimen compliance and associated energy release rate. Correction coefficients were obtained from finite element analysis or analytical models which required various levels of simplification. Crack tip deformation/stress concentration and transverse shear deformation of the adherend are the main reasons why deviations are observed in the Russell and Street analysis, which is deemed to underestimate the energy release rate. Both analytical models and numerical simulations have been proposed to evaluate these effects and to investigate non-linear interface behaviour (Chai, 1992), transverse dimension effects or other artefacts such as crack-lip friction or beam rotation effects (Arrese and Mujika, 2008; Arrese et al., 2010; Sun and Davidson, 2006). None of these works has pursued investigations into strain evolution along the adherend upon which our instrumented ENF test technique is based.

In the present article, we derive a Timoshenko beam model on a two-parameter elastic foundation, as proposed by Shokrieh et al. (2011), Qiao and Wang (2005) and Bennati et al. (2009), for interpreting asymmetric double cantilever beam (ADCB) tests. We concentrate on three point bending experiments on ENF specimens with identical adherends (*viz.* both geometry and material properties). In this configuration, useful analytical expressions are obtained, which exhibit the geometrical and material parameters that control the specimen behaviour. Approximate expressions based on a simplified model are obtained which are useful for data reduction of backface strain monitoring and interface shear compliance identification. Correction coefficients for energy release rate, G_{II}, and specimen compliance are derived. Finally, compressive stress at the crack tip is evidenced which is due to asymmetric loading conditions and/or specimen geometry. This effect is rarely taken into the existing models despite it could delay the fracture due to friction effect.

2. Simple beam theory: beams bonded with an infinitely thin, rigid adhesive

The three point bending End Notched Flexure experiment performed on a bonded joint is shown schematically in Fig. 1. Two identical adherends, of thickness t, width w and length $2L$ are bonded together over most of their length with an adhesive layer of thickness t_a. The two substrates are unbonded from one end over a distance a, designated as the crack length. We concentrate on isotropic and homogeneous materials: E and E_a are respectively the Young's moduli of the adherends and the adhesive, ν and ν_a their Poisson's ratios. The specimen is simply supported at both ends on knife edges and loaded with a concentrated transverse force, P, at its mid-point (homogeneous along w). The specimen is bent and the bondline is aligned with the neutral surface where shear stress in maximal and tensile/compressive stress is zero. As a consequence, pure mode II failure is expected.

The failure onset and ultimate load evaluation of such a specimen is generally based on energy balance considerations as originally proposed by Griffith (Griffith, 1921). The elastic energy stored in the specimen drives the crack propagation, such that the release energy compensates the needs of surface creation, local plastic deformation etc. If linear elastic behaviour is observed at a macroscopic scale, linear elastic fracture mechanics (LEFM) formalism is applicable and the failure criterion is derived from:

$$G = \frac{P^2}{2w}\frac{\partial C}{\partial a} \tag{1}$$

where $C = \delta/P$ is specimen compliance, δ beam deflection, and G the energy release rate. When G attains G_c, the critical energy release rate or fracture energy, depending on material/interface properties, crack propagation occurs. With the traditional analyses, a precise evaluation of specimen compliance is fundamental to allow a correct estimate of G_c.

A preliminary analysis of this experiment (Barrett and Foschi, 1977) was proposed by Russel and Street (1982), for the evaluation of mode II toughness in laminates. In this model, the Euler-Bernoulli beam model was used to describe the bending of the substrates. The adhesive layer was assumed to be infinitely thin, so that the specimen was divided into two parts. Along the bonded area, the specimen behaved as a single beam in bending with thickness $2t$, while along the debonded area, the specimen behaved as two beams in parallel, each of them with thickness t. With this simple beam theory (SBT), the ENF specimen compliance is given by the relation:

$$C = \frac{\delta}{P} = \frac{3a^3 + 2L^3}{8wt^3E} \tag{2}$$

with the associated energy release rate:

$$G_{II} = \frac{9a^2P^2}{16w^2t^3E} \tag{3}$$

Most of the analyses proposed since this early version aim to evaluate the deviation from simple relations by introducing more realistic descriptions of the adhesive and/or adherend behaviour and geometry. Due to bondline and substrate shear compliances, the total compliance of the specimen and energy release rate are higher than predicted by SBT. Nowadays, most of the data reduction techniques use the SBT formula with a corrected value of crack length, which is "artificially" increased so that:

$$C = \frac{\delta}{P} = \frac{3(a + \chi_{II}t)^3 + 2L^3}{8wt^3E} \tag{4}$$

$$G_{II} = \frac{9(a + \chi_{II}t)^2P^2}{16w^2t^3E} \tag{5}$$

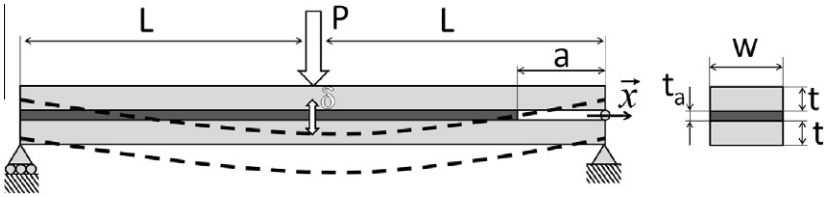

Fig. 1. Geometry of the End Notched Flexure (ENF) experiment.

where the crack length correction is evaluated from numerical or analytical models, many of them being listed in (Yoshihara, 2005).

Other experimental strategies have also been proposed which make use of additional sensors for measuring crack shear displacement (CSD) (Tanaka et al., 1995) or local strain (Yoshihara, 2010), from which additional compliances can be calculated from experimental data. Again, specimen analysis provides a useful relation to retrieve material parameters or crack position. Thus, CSD, or δ_x, and maximal adherend longitudinal strain, ε_x, are given, according to Yoshihara (2005), by relations:

$$\varepsilon_x = \frac{3PL}{4Ewt^2} \tag{6}$$

$$\delta_x = \frac{3P(a+\chi_{II}t)^2}{2Ewt^2} \tag{7}$$

These relations, combined with Eqs. (2) and (3), enable direct computation of energy release rate throughout the experiment, with no need for calculation of any correction coefficients (Yoshihara, 2010). For the following analysis, we recall results from the SBT analysis, which states that both substrates behave as Euler–Bernoulli beams, that the adhesive layer stiffness is infinite, and that the rotation, $\varphi(x)$, and vertical displacement, $v(x)$, are continuous when crossing the frontier between cracked and uncracked portions. The various expressions found for the different zones corresponding to that debonded or crack ($-a < x < 0$), the right hand portion ($-L < x < -a$) and the left hand portion ($-2L < x < -L$) are:

$$\text{rotation:}\quad \varphi(x) = \frac{P}{EI_2}\left(-x^2 + \frac{L^3 - a^3 + 3La^2}{4L}\right) \quad -a < x < 0 \tag{8}$$

$$\varphi(x) = \frac{P}{EI_2}\left(-\frac{x^2}{4} + \frac{L^3 - a^3}{4L}\right) \quad -L < x < -a \tag{9}$$

$$\varphi(x) = \frac{P}{EI_2}\left(\frac{x^2}{4} + Lx + \frac{3L^3 - a^3}{4L}\right) \quad -2L < x < -L \tag{10}$$

$$\text{deflection:}\quad v(x) = \frac{P}{EI_2}\left(-\frac{x^3}{3} + \frac{L^3 - a^3 + 3La^2}{4L}x\right) \quad -a < x < 0 \tag{11}$$

$$v(x) = \frac{P}{EI_2}\left(-\frac{x^3}{12} + \frac{L^3 - a^3}{4L}x - \frac{a^3}{2}\right) \quad -L < x < -a \tag{12}$$

$$v(x) = \frac{P}{EI_2}\left(\frac{x^2}{12} + \frac{Lx^2}{2} + \frac{3L^3 - a^3}{4L} + \frac{L^3}{6} - \frac{a^3}{2}\right) \quad -2L < x < -L \tag{13}$$

$I_2 = 8wh^3/12$ is the second moment of the cross-sectional area in the crack-free portion of the specimen assuming infinite stiffness of the adhesive layer. From these relations, the SBT approximation of the specimen compliance is derived, and also the SBT evaluation of the bending rotation correction coefficients, useful to assess sliding within the contact zone. We can also evaluate the relative sliding of adherends along the cracked portion of the specimen (*cf.* relation (7)).

3. Timoshenko beams on two parameters elastic foundation model

To improve the analysis of the ENF test experiment, it is required to include the influence of the mechanical behaviour of the bondline. In the case of adherends which are thick in comparison with other dimensions (crack length, span length...), the zEuler–Bernoulli formalism is not valid and the Timoshenko beam model should be used instead. Such thick beams are required experimentally to prevent any plastic deformation occurring in the adherends when characterising strong interfaces, which makes analysis of the experiment more complex. In the following analysis, we detail solution for an ENF specimen under three point bending where the test specimen is modelled by two Timoshenko beams bonded with an elastic layer characterised by finite shear and tensile stiffness.

3.1. Constitutive equations

The constitutive equations which rule the local static equilibrium of the adherends and the adhesive layer are based on the model presented in Fig. 2. Local displacements of the cross sections of the beams depends on three independent parameters: the axial, $u_i(x)$, and vertical, $v_i(x)$, displacements of the centre of the cross section, and the cross section rotation $\varphi_i(x)$. In the following, index $i = \pm$ refers to the upper or lower adherend, $s = 1$ for the upper adherend and $s = -1$ for the lower adherend. The local static equilibrium of the bilayer system is expressed by the three usual beam on elastic foundation equations for each of the adherends:

$$\frac{dM_i}{dx} + T_i - \frac{t}{2}w\tau = 0 \tag{14}$$

$$\frac{dT_i}{dx} - sw\sigma = 0 \tag{15}$$

$$\frac{dN_i}{dx} - sw\tau = 0 \tag{16}$$

M_i, T_i and N_i are respectively the local bending moment, shear force and axial force. σ and τ are the normal (or peel) and shear interfacial stresses. Relations (14)–(16) assume that no distributed loads or couples are applied to the upper or lower adherends. According to Timoshenko theory, the constitutive equations for the adherends are:

$$M_i = E_i I_i \frac{d\varphi_i}{dx} \tag{17}$$

$$T_i = \kappa_i G_i S_i \left[\frac{dv_i}{dx} - \varphi_i\right] \tag{18}$$

$$N_i = E_i S_i \frac{du_i}{dx} \tag{19}$$

where E_i and G_i are respectively the Young's and shear moduli of the adherends. $S_i = wt_i$ and $I_i = wt_i^3/12$ are the beam area and second moment of inertia of the beam cross-section and κ_i is the shear correction coefficient. $\kappa_i \approx 5/6$ is an acceptable value in the case of a rectangular cross section (Timoshenko, 1921). Linear elastic behaviour is assumed for the bondline, so that the interfacial stresses are proportional to the normal and tangential relative displacements of the interface:

$$\sigma = \frac{E_a^*}{t_a}[v_+ - v_-] \tag{20}$$

$$\tau = \frac{G_a}{t_a}\left[\frac{t}{2}[\varphi_+ + \varphi_-] + u_+ - u_-\right] \tag{21}$$

with:

$$E_a^* = \frac{E_a(1-\nu_a)}{(1+\nu_a)(1-2\nu_a)} \tag{22}$$

$$G_a = \frac{E_a}{2(1+\nu_a)} \tag{23}$$

where t_a is the adhesive layer thickness, and E_a, G_a and ν_a are respectively the Young's modulus, shear modulus and Poisson's

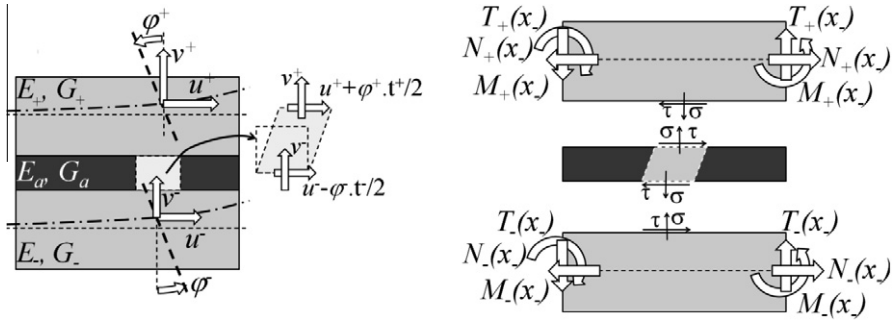

Fig. 2. Kinematic and static description of two beams with an adhesive connecting layer.

ratio of the adhesive. In Eqs. (20) and (22), the apparent value, E_a^*, of the adhesive Young's modulus is introduced to take into account the enhanced tensile rigidity of the bondline due to its plane strain condition. In Eqs. (20) and (21), we use the classical approximation originally proposed by Volkersen (1938) and Goland et al. (1944). These approximations generally overestimate the peak stress at the end of the joint and thus allow conservative design. A list of more sophisticated models can be found in (da Silva et al., 2009), in which is pointed out the need for a finer description of the mechanical field heterogeneity through the thickness, and the stress free condition. This was previously discussed by Adams and Peppiatt (1974). Nevertheless, at a mesoscopic level, and in the case of a thin and soft adhesive layer, the classic approach would seem satisfactory to evaluate global response of the joint (Goglio and Rossetto, 2011). It is hoped that the experimental technique developed in part II of this work will prove sensitive enough to show some effects that may be predicted with more advanced mechanical models of interfaces (Zhao et al., 2011; Luo and Tong, 2009) or of adherends (Raghu Prasad and Pavan Kumar, 2008; Shokrieh et al., 2012). Ultimately, the problem is described by a set of six coupled differential equations, which cannot be solved analytically unless the adherends are identical. Numerical analysis of such a bonded bi-layer system has been presented by Bennati et al. (2010). Surprisingly, this numerical method is not directly applicable to a symmetric bonded joint. Indeed, by combining Eqs. (14)–(23), we obtain two coupled sixth order differential equations in σ and τ. No simple analytical expression for the roots of the characteristic equation of this differential system has been found so that numerical solution is required. In the case of similar adherends, we obtain two independent homogeneous linear differential equations in σ and τ:

$$0 = \frac{t_a}{E_a^*}\frac{d^4\sigma}{dx^4} - 2\frac{w}{\kappa GS}\frac{d^2\sigma}{dx^2} + \frac{2w}{EI}\sigma \tag{24}$$

$$0 = -\frac{t_a}{G_a}\frac{d^3\tau}{dx^3} + 2w\left[\frac{1}{EI}\left(\frac{t}{2}\right)^2 + \frac{1}{ES}\right]\frac{d\tau}{dx} \tag{25}$$

where G, E, I, S and κ refer respectively to the adherend shear modulus, Young's modulus, quadratic moment, section and shear correction coefficient, which are now equal for upper and lower adherend. Eqs. (24) and (25) exhibit three double roots for the characteristic equation, while in the case of dissimilar adherends six different roots are obtained. With these double roots, a specific inversion procedure must be proposed. As a result, analytical expressions for the parameters which drive the experiment are found, with the evolution of shear and tensile stress in the adhesive layer.

Thus, according to the differential Eq. (24), the tensile stress distribution is controlled by two "wave numbers" $\lambda_{\sigma 1}$ and $\lambda_{\sigma 2}$:

$$\sigma(x) = F_1 exp(\lambda_{\sigma 1}x) + F_2 exp(-\lambda_{\sigma 1}x) + F_3 exp(\lambda_{\sigma 2}x) + F_4 exp(-\lambda_{\sigma 2}x) \tag{26}$$

Similarly, the shear stress distribution depends on only one wave number λ_τ:

$$\tau(x) = F_5 exp(\lambda_\tau x) + F_6 exp(-\lambda_\tau x) + \tau_m \tag{27}$$

where coefficient, F_k, and mean shear stress, τ_m, depend on the boundary conditions on both sides of the bonded bi-layer structure. Contrary to the case of dissimilar adherends, analytical expressions can be found for the wave numbers $\lambda_{\sigma 1}$, $\lambda_{\sigma 2}$ and λ_τ. These parameters are important since they control the stress distribution along the adhesive layer. Writing:

$$k_z = w\frac{E_a^*}{t_a} \tag{28}$$

$$k_x = w\frac{G_a}{t_a} \tag{29}$$

The three wave numbers are solutions of the characteristic polynomial of the differential equations (24) and (25):

$$\lambda_{\sigma i} = \lambda\sqrt{2\left(\mu \pm \sqrt{\mu^2 - 1}\right)} \tag{30}$$

$$\mu = \frac{\sqrt{2k_z EI}}{2\kappa GS} \tag{31}$$

$$\lambda = \frac{\sqrt{2}}{2}\left(\frac{2k_z}{EI}\right)^{1/4} \tag{32}$$

$$\lambda_\tau = \sqrt{2k_x\left(\left(\frac{t}{2}\right)^2\frac{1}{EI} + \frac{1}{ES}\right)} \tag{33}$$

In the following, we will use the notation $\lambda_1 = \lambda_{\sigma 1}$, $\lambda_2 = -\lambda_{\sigma 1}$, $\lambda_3 = \lambda_{\sigma 2}$, $\lambda_4 = -\lambda_{\sigma 2}$, $\lambda_5 = \lambda_\tau$, $\lambda_6 = -\lambda_\tau$, to make the expression more compact. We replace $\sigma(x)$ and $\tau(x)$ by their expressions in relations (14)–(19), and integrate to obtain a general expression for internal forces $[N_i(x), T_i(x), M_i(x)]$ and displacements $[u_i(x), v_i(x), \varphi_i(x)]$ along upper and lower adherends:

$$T^i(x) = s\sum_{k=1}^{4} w\frac{F_k}{\lambda_k}exp(\lambda_k x) + A_i \tag{34}$$

$$M^i(x) = -s\sum_{k=1}^{4} w\frac{F_k}{\lambda_k^2}exp(\lambda_k x) + \frac{t}{2}\sum_{k=5}^{6} w\frac{F_k}{\lambda_k}exp(\lambda_k x) + \left(\frac{t}{2}w\tau_m - A_i\right)x + B_i \tag{35}$$

$$\varphi^i(x) = \frac{1}{EI}\left\{-s\sum_{k=1}^{4} w\frac{F_k}{\lambda_k^3}exp(\lambda_k x) + \frac{t}{2}\sum_{k=5}^{6} w\frac{F_k}{\lambda_k^2}exp(\lambda_k x) + \frac{1}{2}\left(\frac{t}{2}w\tau_m - A_i\right)x^2 + B_i x\right\} + C_i \tag{36}$$

$$v^i(x) = \frac{1}{EI}\left\{-s\sum_{k=1}^{4} w\frac{F_k}{\lambda_k^4}exp(\lambda_k x) + \frac{t}{2}\sum_{k=5}^{6} w\frac{F_k}{\lambda_k^3}exp(\lambda_k x) + \frac{1}{6}\left(\frac{t}{2}w\tau_m - A_i\right)x^3 + \frac{1}{2}B_i x^2\right\} + \left(C_i + \frac{A_i}{\kappa GS}\right)x + D_i + \frac{s}{\kappa GS}\sum_{k=1}^{4} w\frac{F_k}{\lambda_k^2}exp(\lambda_k x) \quad (37)$$

$$N^i(x) = s\left[w\tau_m x + \sum_{k=5}^{6} w\frac{F_k}{\lambda_k}exp(\lambda_k x)\right] + E^i \quad (38)$$

$$u^i(x) = \frac{1}{ES}\left[s\left(w\tau_m\frac{x^2}{2} + \sum_{k=5}^{6} w\frac{F_k}{\lambda_k^2}exp(\lambda_k x)\right) + E^i x\right] + G^i \quad (39)$$

Constants A_i, to G_i depend on the boundary conditions and must also fulfil the conditions (20) and (21), so that seven additional compatibility equations are found. In the case of identical adherends we obtain:

$$A_+ = A_- = \left(\frac{t}{2} + \frac{2}{t}\frac{I}{S}\right)w\tau_m \quad (40)$$

$$B_+ = B_- = -\frac{1}{t}\frac{I}{S}(E^+ - E^-) \quad (41)$$

$$C_+ = C_- \quad (42)$$

$$D_+ = D_- \quad (43)$$

$$2C\frac{t}{2} + G^+ - G^- - \frac{t_a}{G_a}\tau_m = 0 \quad (44)$$

To achieve a solution to this problem, boundary conditions must be taken into account. In the present work, we use standard assumptions for the ENF analysis. The lower beam is simply supported on its two ends and a transverse force is applied in the middle of the upper beam. As shown in Section 2, the structure is divided into three regions for analysis: $-2L < x < -L$; uncracked portion of the specimen between left end and applied load, $-L < x < -a$; also bonded, and $-a < x < 0$; a cracked, or separated part. Along the separated zone of the specimen, a simple interface model is used since we set the interface rigidity to zero, assuming no interaction (friction or stiffness) to occur between the adherends. Along the cracked part of the specimen, the evolution of internal forces and displacement fields are given by the usual relations:

$$T^i(x) = A_i \quad (45)$$

$$M^i(x) = -A_i x + B_i \quad (46)$$

$$\varphi^i(x) = \frac{1}{EI}\left\{-\frac{1}{2}A_i x^2 + B_i x\right\} + C_i \quad (47)$$

$$v^i(x) = \frac{1}{EI}\left\{-\frac{1}{6}A_i x^3 + \frac{1}{2}B_i x^2\right\} + \left(C_i + \frac{A_i}{\kappa GS}\right)x + D_i \quad (48)$$

$$N^i(x) = E^i \quad (49)$$

$$u^i(x) = \frac{1}{ES}\left[E^i x\right] + G^i \quad (50)$$

Fifty integration constants need to be calculated by inversing a linear system consisting of 24 continuity equations at $x = -a$ and $x = -L$, 14 compatibility conditions and 12 boundary conditions at $x = -2L$ and $x = 0$. This operation is done numerically since no simple analytical expression has been found for solution of the complete problem. As a result, interface stresses are computed using relations (26) and (27), and mode I and mode II components of the energy release rate which drives the fracture are computed with the classical relations used in (Bennati et al., 2009):

$$G_I = \frac{\sigma_a^2}{2E_a^*}t_a \quad (51)$$

$$G_{II} = \frac{\tau_a^2}{2G_a}t_a \quad (52)$$

These relations are computed from the following expression for the J integral assuming linear behaviour of the adhesive layer:

$$J = J_I + J_{II} = \int_0^{\delta^*}\sigma(\delta)d\delta + \int_0^{\gamma^*}\tau(\gamma)d\gamma \quad (53)$$

where δ and γ denote the normal and tangential relative displacement of the interfaces at the crack tip positions. Based on relation (53), a measurement technique (Sørensen and Jacobsen, 2003) has been developed for measuring the non linear behaviour of interfaces under mixed mode loading (Lundsgaard-Larsen et al., 2008; Sørensen and Jacobsen, 2009) which could probably be improved by using it in combination with the methodology developed in the two present articles.

During the experiment, negative values of σ are to be expected. Since the crack in mostly driven by shear, any compressive stress is expected to retard fracture due to friction. This effect is neglected in the present analysis. When the crack tip is loaded in compression, no mode I stress singularity component is expected and $G_I = 0$. Consequently, the ENF test remains a pure mode II fracture mechanics test. Rather than the mode mixity ratio, it is important to estimate the remote stress ratio at the crack tip, τ/σ, which must be carefully considered when analyzing the damage process during crack propagation.

3.2. Simplified model of ENF test for the analysis of strain gauge monitoring

Backface strain instrumentation enables precise monitoring of crack propagation and stress distribution in the region of the adhesive layer at the crack front. For the ENF test pieces, strain gauges are bonded to the outer sides of the upper and/or lower adherends in order to measure the local, longitudinal strain, which is given by the relation:

$$\varepsilon_{li} = \frac{N_i}{E_i S_i} - s\frac{M_i}{E_i I_i}\frac{t_i}{2} = \frac{du_i}{dx} - s\frac{d\varphi_i}{dx}\frac{t_i}{2} \quad (54)$$

Expressions for local beam rotation (36) and axial displacement (38) are rather complicated and the analytical relation, based on an approximate model such as that presented in Fig. 3, is an idealised representation of the bonded region of the cracked side of the specimen ($-L < x < -a$) or ($-d < x^* < 0$), with $x^* = x + a$.

In the ideal representation of the ENF test, the load is equally shared between upper and lower substrates so that no peel stresses are produced in the adhesive layer. In such a situation, ENF can be regarded as a pure mode II test. The problem can be decomposed into two elementary problems.

Case 1: two equal shear forces $T^i = F$ are applied to the right-hand end of the beam, in which case:

$$A_+ = A_- = F \quad (55)$$

$$B_+ = B_- = 0 \quad (56)$$

$$E_+ = E_- = 0 \quad (57)$$

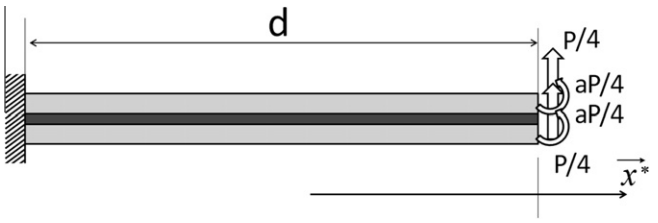

Fig. 3. Simplified model of the bonded zone.

$$\tau_m = F\frac{2St}{\left(4I+St^2\right)w} \tag{58}$$

$$F_5 = F\frac{-St}{\left(4I+St^2\right)w}\frac{1}{cosh(\lambda_\tau d)} \tag{59}$$

$$F_6 = F\frac{-2St}{\left(4I+St^2\right)w}\frac{1}{cosh(\lambda_\tau d)} \tag{60}$$

Case 2: two equal bending moment M are applied to the right end of the beam, other coefficients are given by the relations, giving:

$$A_+ = A_- = 0 \tag{61}$$

$$B_+ = B_- = \frac{4I}{4I+St^2}M \tag{62}$$

$$E_+ = E_- = \frac{-2St}{\left(4I+St^2\right)}M \tag{63}$$

$$\tau_m = 0 \tag{64}$$

$$F_5 = \frac{St\lambda_\tau}{\left(4I+St^2\right)w}\frac{exp(\lambda_\tau d)}{cosh(2\lambda_\tau d)}M \tag{65}$$

$$F_6 = -\frac{St\lambda_\tau}{\left(4I+St^2\right)w}\frac{exp(-\lambda_\tau d)}{cosh(\lambda_\tau d)}M \tag{66}$$

From these expressions, when applying the boundary conditions described in Fig. 3, we find the shear stress distribution:

$$\tau(x) = \frac{P}{4tw}\frac{2St^2}{4I+St^2}\left\{1-\frac{cosh(\lambda_\tau x)}{cosh(\lambda_\tau d)}+\lambda_\tau a\frac{sinh(\lambda_\tau(d+x))}{cosh(\lambda_\tau d)}\right\} \tag{67}$$

Also found is the evolution of the bending moment and the axial force along the adherend:

$$M^i(x) = \frac{P}{4}\left\{\frac{4I(a-x)}{4I+St^2}+\frac{St^2}{4I+St^2}\left[-\frac{1}{\lambda_\tau}\frac{sinh(\lambda_\tau x)}{cosh(\lambda_\tau d)}+a\frac{cosh(\lambda_\tau(d+x))}{cosh(\lambda_\tau d)}\right]\right\} \tag{68}$$

$$N^i(x) = \frac{P}{4t}\frac{2St^2}{4I+St^2}\left\{x-a-\frac{1}{\lambda_\tau}\frac{sinh(\lambda_\tau x)}{cosh(\lambda_\tau d)}+a\frac{cosh(\lambda_\tau(d+x))}{cosh(\lambda_\tau d)}\right\} \tag{69}$$

Using expressions (52) and (67), we may calculate the energy release rate:

$$G_{II} = \frac{9a^2P^2}{16Ew^2t^3}\left[\frac{1}{\lambda_\tau a}\left(1-\frac{1}{cosh(\lambda_\tau d)}\right)+tanh(\lambda_\tau d)\right]^2 \tag{70}$$

which can be approximated by the following formula in the case $\lambda_\tau d \gg 1$:

$$G_{II} \approx \frac{9a^2P^2}{16Ew^2t^3}\left[\frac{1}{\lambda_\tau a}+1\right]^2 \tag{71}$$

These expressions are similar to those proposed with corrected beam theory (Blackman et al., 2005), in which the interface compliance is taken into account through an effective crack length correction, and by using a correction factor to take into account additional artefacts such as large displacements. It should be noted that with the classical method, the crack length correction remains constant during the whole experiment, while according to relation (71), the correction varies during propagation since it depends on the coefficient $\lambda_\tau a$.

Finally, and importantly from the experimental standpoint, an approximate solution for longitudinal skin strain distribution is also found:

$$\varepsilon_l(x) = \frac{P}{4EI}t\left\{\frac{4I(x-a)}{4I+St^2}+\frac{1}{2}\frac{4I-St^2}{4I+St^2}\left[-\frac{1}{\lambda_\tau}\frac{sinh(\lambda_\tau x)}{cosh(\lambda_\tau L)}+a\frac{cosh(\lambda_\tau(L+x))}{cosh(\lambda_\tau L)}\right]\right\} \tag{72}$$

$$\varepsilon_l(x) \approx \frac{P}{4EI}t\left\{\frac{4I(x-a)}{4I+St^2}+\frac{1}{2}\frac{4I-St^2}{4I+St^2}a.exp(\lambda_\tau x)\right\} \tag{73}$$

4. Analysis of three point bending ENF test

In the following, we analyse the stress/strain evolution in a symmetric ENF specimen loaded by three point bending, as determined from the models presented in Sections 2 and 3 (*viz.* SBT, explicit ENF, simplified ENF). Isotropic homogenous adherends (E = 70 GPa, ν = 0.3) of thickness t = 5 mm, width w = 25 mm and span length $2L$ = 180 mm are considered. We assume a 1000 μm thick bondline and a relatively rigid ($E_a \approx 5$ GPa, $\nu_a \approx 0.3$) structural adhesive. This configuration is very common and representative of that tested in the second part of this work. With the coefficients proposed, characteristic distances are: $1/\lambda_{\sigma 1} \approx 1/\lambda_{\sigma 2} \approx 3.2$ mm and $1/\lambda_\tau \approx 4.8$ mm. Crack length, a, corresponding to the length of the debonded part, is 70 mm. All calculations are done for unit applied load. From this analysis, new test and experimental data reduction protocols can be proposed for a refined evaluation of the energy release rate and interface compliance In the following, all quantities are represented as a function of $X = x + L$ so that the origin of the axis is now located at the mid-span position.

In Fig. 4 are represented the evolution of the components of adherend displacement and rotation along the span, determined with the complete ENF model and compared with the SBT solution [*viz.* Eqs. (8)–(13)]. The influence of interface compliance is clearly visible since the deflection predicted with the bonded bi-layer model is significantly higher than that given by relation (2). Correspondingly, variation of beam rotation is also more spread out with the elastic interface. The evolution of longitudinal displacement along the neutral surface of each adherend is also different from that evaluated with the SBT approximation. As expected, the horizontal, relative displacement on the left-hand side of the specimen is greater with an elastic interface. At the crack front, the opposite trend is observed, which is not surprising since the SBT approximation does not allow for any root rotation effects.

In Fig. 5 is represented the evolution of internal forces in the adherend along the span. These quantities are easier to evaluate than the kinematic variables plotted in Fig. 4, since they are very similar to those predicted by the SBT model. The mean shear force value is close to ±P/4 in each adherend, which demonstrates that, despite non-symmetric loading conditions, the force is almost equally shared in the two adherends except near the edge of the bonded area and in the middle of the specimen where interaction

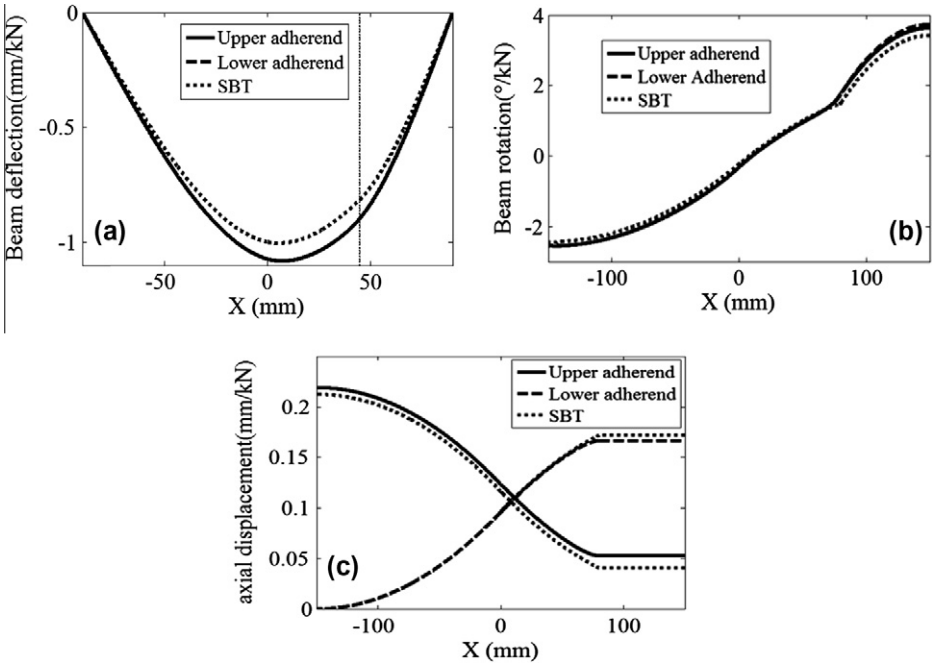

Fig. 4. Evolution of (a) adherend deflection, v_i, (b) rotation, φ_i, and (c) longitudinal displacement, u_i, along the span. Crack length $a = 70$ mm.

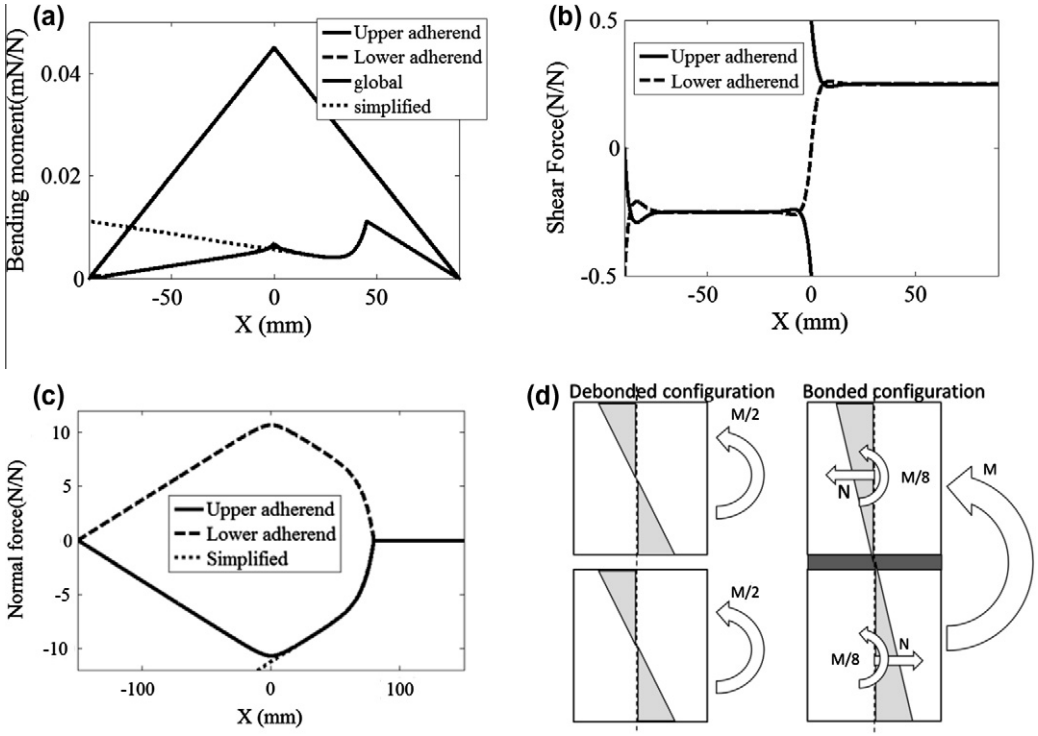

Fig. 5. Evolution of bending moment (a), shear (b) and axial (c) forces in adherend along the span, $a = 70$ mm.

with the crack or the grips occurs. It should be noted that along the debonded part of the specimen, the upper and lower adherends sustain identical transverse loads which indicates no tensile or compressive stress at the crack tip. Examination of evolution of bending moment and axial forces evolutions in the upper and lower adherends (see Fig. 5) also illustrates how internal forces are changed from a pure bending moment in the debonded part of the specimen into a combination of tension/compression and bending along the bonded zone. This stress distribution is similar to that predicted by SBT except in the vicinity of the crack tip loading so that:

$$M_{free} = \frac{M}{2} = 4M_{bonded} \quad N_{bonded} = \frac{3M}{4t} \tag{74}$$

where M is the local macroscopic bending moment [$-Px$ or $P(2L + x)$]. M_{free} and M_{bonded} are respectively the bending moment

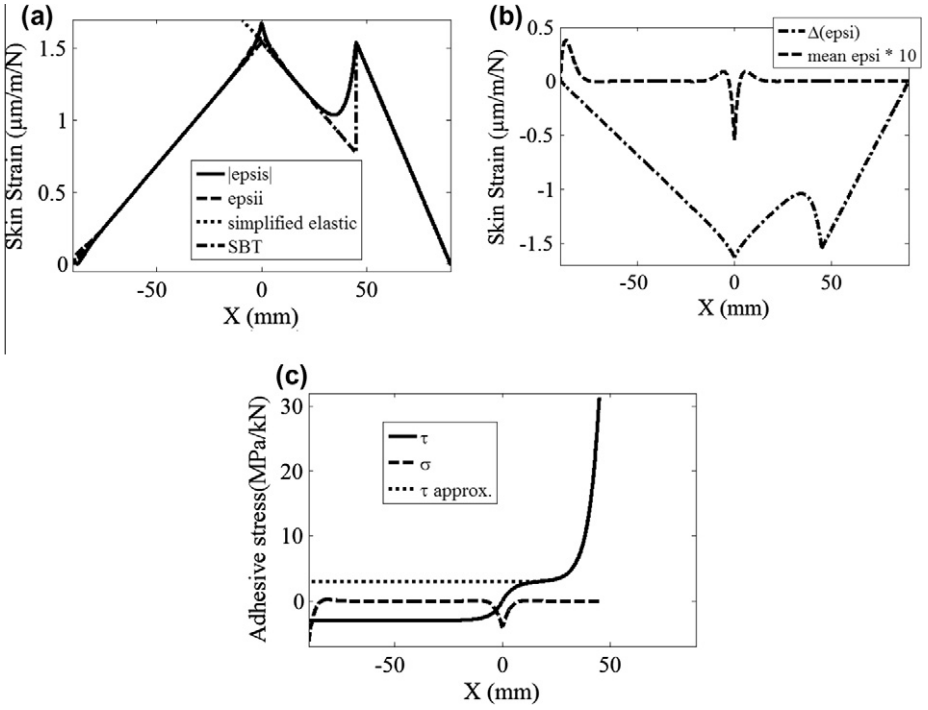

Fig. 6. (a) Skin strain evolution along the span, (b) evolution of sum and difference of lower and upper skin strain along the span, (c) resulting shear and peel stress distribution along the span.

in the adherend along the debonded and bonded parts and N_{bonded} is the axial force in the bonded part.

In Fig. 6 are represented the quantities to be measured in a backface strain monitoring version of the ENF experiment. These additional measurements should enable a finer investigation of the stress distribution in the adhesive layer, and in particular in the vicinity of the crack tip where an important gradients are observed. The mean shear stress, τ_m, in the adhesive is given by relation (58). Peak compressive stresses are observed at the loading pins positions. The length affected by these compressive stresses is $\approx 1/\lambda_{\sigma i}$. These unexpected stresses appear because the forces are locally applied on one adherend only and thus in an asymmetric way. Similarly, to accommodate the conversion from bending load to combined bending and tension/compression load in the adherend, a large shear stress gradient appears in front of the crack tip. The gradient is controlled by the parameter λ_τ and excellent agreement is observed with the evolution predicted from the simplified model. Longitudinal strain along the upper and lower adherends is evaluated using relation (54). According to SBT, at the same position along the span, the strain is twice as big if the two adherends are debonded, compared to the bonded configuration.

$$|\varepsilon_{free}| = \frac{Px}{4EI}\frac{t}{2} \quad |\varepsilon_{bonded}| = \frac{Px}{4EI}\frac{t}{4} \tag{75}$$

This trend is also predicted by the simplified model and is confirmed by the complete model simulations which also reveal a smooth transition between these two regimes, due to shear stress gradient controlled by the λ_τ parameter. Again, the full model is in good agreement with the simplified model. In the configuration tested, the crack location is far enough from the loading position so that negligible interaction is expected between the compressive zones and the process zone in front of the crack tip. The experimental results to be presented in the second part of this work, show an antisymmetric contribution which is not predicted with the simplified model in which only pure symmetric loading is considered. This asymmetric contribution is associated with a compressive load at the crack tip, or tendency for crack closure. To separate and distinguish between crack closure compressive stress and mode II contributions, a simple method consists of calculating the difference and the mean values of the strains observed at the same location along the span on the upper and lower skin of the specimen. With this operation, we do not directly probe the local cohesive force, but separate the component of deformation of the specimen due to symmetric loading with respect to the bondline (*viz.* mode I) from that due to antisymmetric loading (*viz.* mode II). Once isolated, these two contributions to the bondline properties can be evaluated from equation (73) using the simplified analysis proposed in Section 3.2, to be explained in detail in part II.

The backface strain monitoring technique has been used with a double cantilever beam Mode I crack propagation experiment and has enabled quantitative evaluation of the $\lambda_{\sigma i}$ parameters (Budzik et al., 2011a,b; Ben Salem et al., 2012). The same approach should be possible here except that with mode II loading, λ_τ should be obtained rather than $\lambda_{\sigma i}$.

Most of the data reduction techniques developed for analysis of ENF tests are based on the use of crack length correction. With our calculations, (a) crack length and (b) energy release rate correction coefficients are obtained which are defined by the following equations:

$$C_G = \frac{G_{SBT}}{G} \tag{76}$$

$$C_a = \frac{a}{a_{app}} \tag{77}$$

The apparent crack position evaluated using the SBT compliance formula is given by:

$$a_{app} = \sqrt[3]{\frac{1}{3}\left(8wt^3E\frac{\delta}{P} - 2L^3\right)} \tag{78}$$

The evolution of coefficients C_a and C_G with the geometrical crack length are shown in Fig. 7.

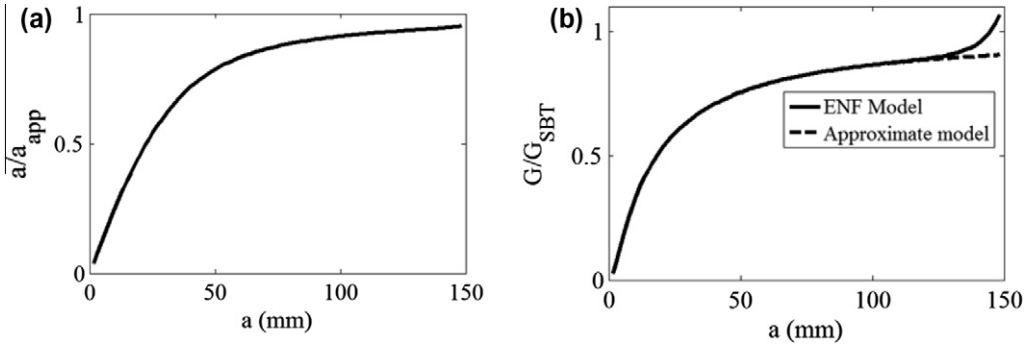

Fig. 7. Correction coefficients for (a) a crack length, (b) energy release rate.

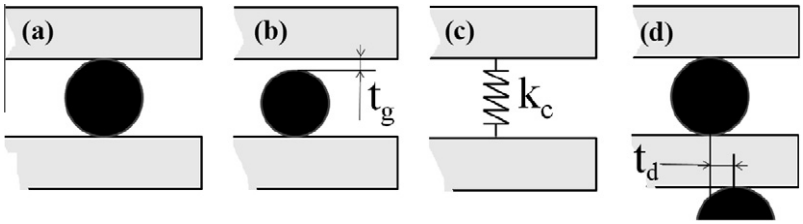

Fig. 8. Origin of mode I (crack closure) contribution. (a) ideal conditions, (b) different bondline and spacer stiffness, (c) contact finite stiffness, (d) misalignment between loading pin and spacer.

In relation (76), the global energy release rate G is calculated numerically using Eq. (1), so that the compressive stresses in the adhesive at the loading pin positions are also taken into account in the energy balance.

The correction coefficients indicate that for a short crack, an important error is made in the estimated crack position due to the higher compliance of a real specimen compared to that due to interface elasticity. Similarly, the estimated energy release rate is smaller than the real value so that by using apparent values of crack position instead of the geometrical ones, auto correction is to some extent achieved. It should also be noted that the approximate function for energy release rate (71) is most satisfactory except at the moment when the crack approaches the middle of the span, where some interaction occurs between the stress redistribution zone in front of the crack tip and the compression zone due to applied load.

5. Compressive stress at the crack tip – Crack closure

The backface strain measurement technique, which is presented in the second part of this article shows that specimen deformation is not purely asymmetric with respect to the bondline. The symmetric contribution is associated to a significant compressive stress at the crack tip crack or crack closure effect.

5.1. Boundary condition – experimental artefact

Such an artefact can be attributed to an imperfect boundary condition on the debonded side of the specimen, as illustrated in Fig. 8. In practice, equal adhesive bondline and spacer thicknesses but most of all infinite contact stiffness are difficult to achieve. Hertzian contact and imperfect alignment between spacer and loading pin position lead to finite stiffness, which can be roughly evaluated in our configuration with the following relations.

Assuming Hertzian contact between a cylinder and a plane, the compliance is given by:

$$\frac{\delta}{P}=\frac{1}{k_c}=\frac{2}{w}(V_s+V_r)\left[1+ln\left\{\frac{2w^3}{P\emptyset(V_s+V_r)}\right\}\right] \tag{79}$$

where ø is the diameter of the rod and:

$$V_s=\frac{1-\nu^2}{\pi E}\quad V_s=\frac{1-\nu_r^2}{\pi E_r} \tag{80}$$

E_r and ν_r are Young's modulus and Poisson's ratio of the rod. The stiffness due to the gap between spacer and loading pin is estimated from the relation:

$$k_{gap}=G\frac{wt}{t_d} \tag{81}$$

In Fig. 9, are presented the main evolutions, which differ from that presented in Figs. 4–6, when a gap exists between the upper adherend and the spacer. In this case, the debonded upper adherend displacements are controlled by displacement and rotation at the crack tip position up to the moment when the left end touches the spacer. In the meantime, the shear stress along this part is equal to zero, and due to this dissymmetric loading, a significant compressive stress is observed at the crack tip. The peel stress component is much higher than the shear stress, which indicates that this test is sensitive to edge boundary conditions. By calculating the mean $\Sigma\varepsilon=(\varepsilon_{l+}+\varepsilon_{l-})/2$ and difference $\Delta\varepsilon=(\varepsilon_{l+}-\varepsilon_{l-})/2$ of longitudinal strain along the adherend, symmetric and antisymmetric (viz. mode II) contributions can be separated. We notice that, despite abnormal loading conditions, the mode II contribution remains the same as that predicted with the simplified model, and consequently, the same as that obtained with ideal boundary conditions. This result is expected since only linear elastic behaviour is considered. On the contrary, a significant symmetric contribution is observed. Indeed, despite the $\Sigma\varepsilon$ evolution being similar to that predicted for DCB tests, the sign of the strain associated with the symmetric contribution is opposite in our case. It indicates compression at the crack tip and thus a crack closure mechanism, rather than crack opening which provokes failure. This is an

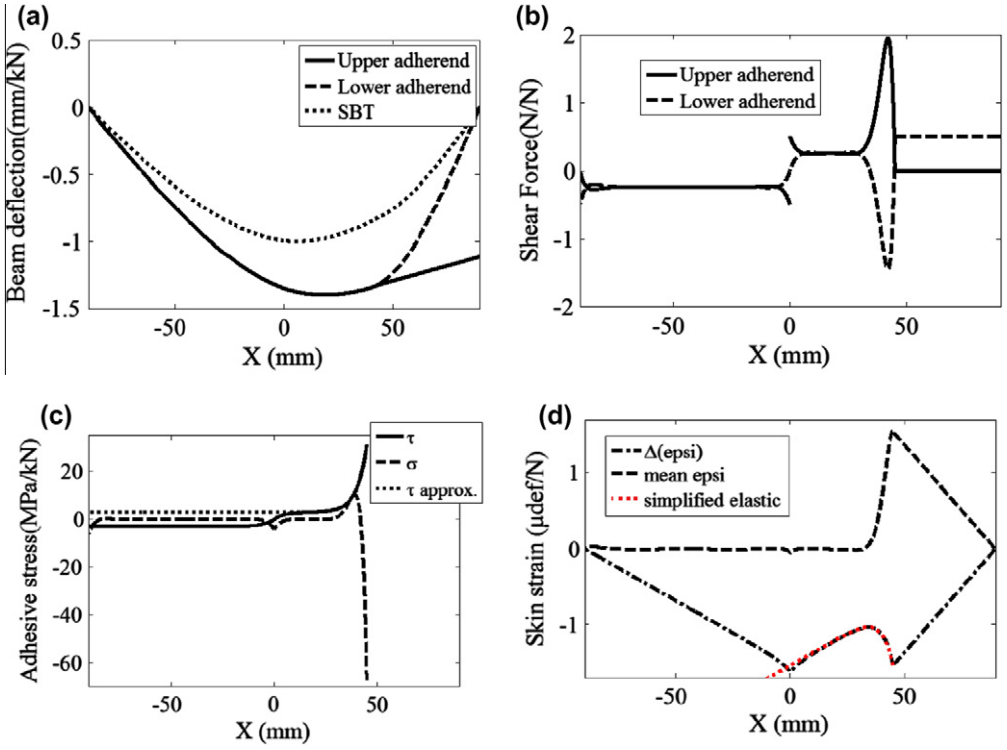

Fig. 9. Mode I contribution, (a) beam deflection, (b) shear forces in the adherends, (c) shear and peel adhesive stresses, (d) mean and difference between upper and lower longitudinal strain.

important result in itself in terms of understanding the three point bending ENF test. Indeed, the sensitivity to compressive stress would be certainly different in case of non linear behaviour.

For complete simulation of the experiment, a new elastic boundary condition should be used when the upper adherend touches the spacer:

$$T^+(x=0) = k_c\left[v^+(x=0) + t_g\right] \tag{82}$$

with this configuration, two limit configurations should be considered. In case of infinite stiffness, the upper adherend deflection remains constant during the experiment, $v^+(x=0) = -t_g$, provided the applied load is sufficient to maintain contact. In the case of low rigidity, the upper adherend is not constrained, which corresponds to the configuration presented in Fig. 8.

5.2. Effect of attached adhesive after failure

Along the fractured part of the specimen, an adhesive coating remains at the lower surface of the upper adherend and on the upper surface of the lower adherend corresponding to adhesive fracture within the adhesive layer, whose mechanical contribution on the global or local behaviour of the specimen is rarely taken into account. In case of significant adhesive thickness and rigidity, a non-negligible increase of the bending rigidity is expected, accompanied by an offset of the effective neutral axis with respect to (at least) one of the adherends. As a consequence, bending and shear rigidity should be replaced by (Roark et al., 2002):

$$\kappa GS_{eff} = \kappa GS + \kappa G_a w t_c \tag{83}$$

$$EI_{eff} = \frac{w\left(E_a^2 t_c^4 + E^2 t^4 + 2t_c t E_a E\left(2t^2 + 3tt_c + 2t_c^2\right)\right)}{12(t_c E_a + tE)} \tag{84}$$

where t_c is the coating adhesive thickness. The neutral axis is translated toward the coating side by a distance:

$$\Delta y_N = -\frac{t_c E_a (t + t_c)}{2(t_c E_a + tE)} \tag{85}$$

Two extreme configurations should be considered depending on whether the fracture is cohesive within the adhesive or interfacial (*viz.* Fig. 10). In case of purely cohesive fracture, the crack front is assumed to propagate along the midplane of the adhesive layer so that apart from boundary conditions effects, the specimen and the experiment remain asymmetrical. In the case of adhesive fracture, the crack front propagates along one of the interface between the adherend (upper or lower) and the adhesive layer, so that the bending rigidity of one of the adherends is enhanced (rather than both).

During the experiment, the adherends remain almost parallel. To obtain similar beam deflection for the two members of the cracked part of the specimen, the shear force should be higher in the adherend with residual adhesive, since both shear and bending rigidity are higher. Modelling the description of the transition between the bonded and cracked parts of the specimen with a discontinuity between coated beams and the thick beam on its elastic foundation is rather delicate and higher order beams (Reddy et al., 1997) or laminates (Murthy et al. 2005) should be implemented for a more precise description of mechanical fields in the vicinity of the crack tip. Nevertheless, some interesting trends are obtained with this simple model which, as we believe, are observed experimentally with the backface strain monitoring technique to be described in part II of this work. Indeed, the dissymmetry induced by adhesive failure near the upper adherend also contributes to the crack closure mechanism since compressive stress are observed. In addition, the change of position of the neutral axis at the transition between the bonded part of the specimen and the cracked part produces a rapid variation (discontinuity in the case of the analytical model) of the backface strain, which is clearly visible when calculating the sum of the longitudinal strains measured on the outer side of the upper and lower adherends. Finally, it

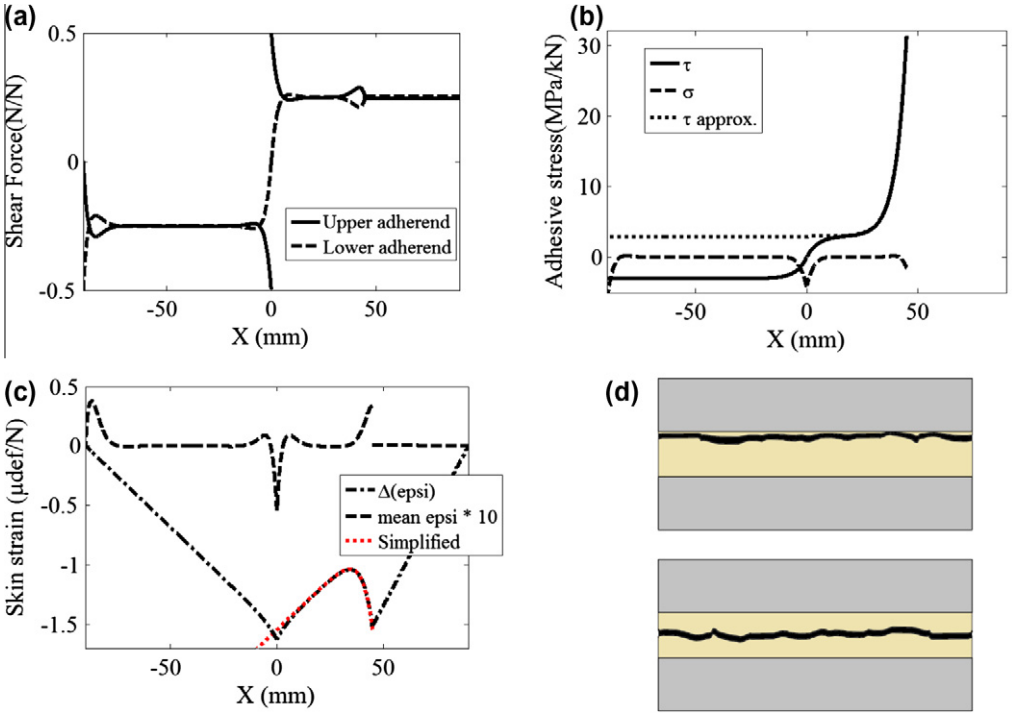

Fig. 10. Effect of adhesive failure. (a) Shear force in the adherend, (b) adhesive shear and peel stress, (c) mean and difference of longitudinal strains, (d) schematic of virtually adhesive (interfacial) failure and cohesive failure within the adhesive.

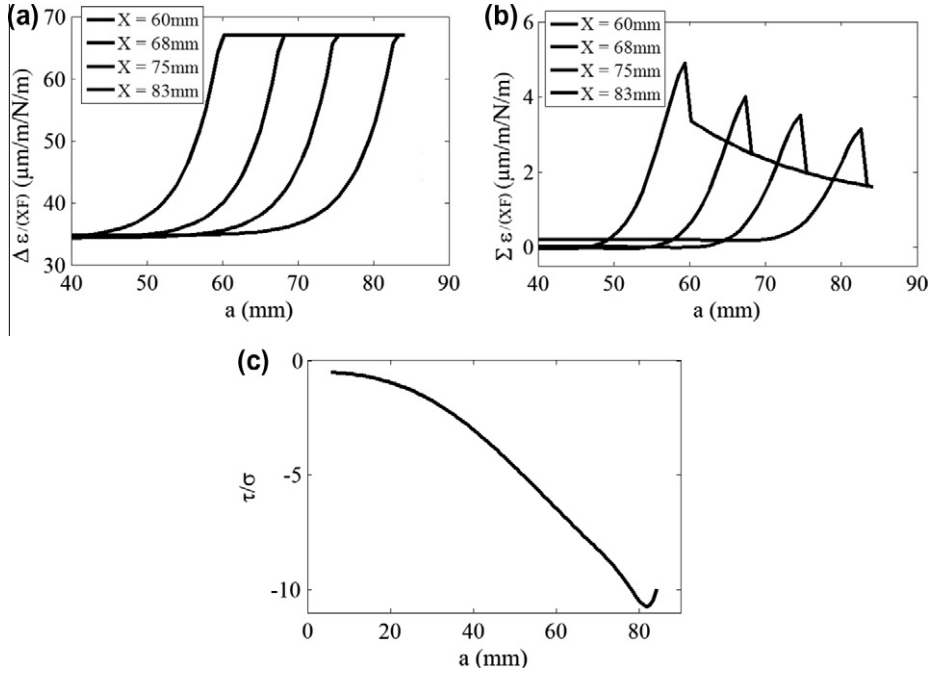

Fig. 11. Simulation of backface monitoring measurement in case of imperfect experimental conditions: (a) difference of longitudinal strain measurements, (b) sum of longitudinal strain measurements, (c) stress ratio.

should be noted that, despite the induced dissymmetry, the mode II contribution remains unchanged, and the simplified model proposed in Section 3.2 fits the shear stress distribution along the bondline as well as the evolution of $\Delta\varepsilon=(\varepsilon_{l+} - \varepsilon_{l-})/2$. This illustrates again the ability of this method to 'filter' the artefact of asymmetry and isolate the mode II contribution only. Similarly, the sum of strain values along the bonded region exhibits the same evolution as that observed during a DCB test which is generally associated to a mode I contribution. However, the positive value of $\Sigma\varepsilon$ indicate crack closure effect rather than mode I contribution. Finally, it should observed that despite the strain level is much weaker than the one associated to Mode II, the compressive stress might be significant compare to the shear stress.

To conclude, the evolution of normalised longitudinal strain (mean and deviation) along the crack propagation is simulated in the case of soft contact ($k_c = 2.10^6$), a 10 μm gap and adhesive

failure along the bondline/upper adherend interface. Results are presented in Fig. 11. The main features which are observed experimentally in part II of this work are shown. The normalised difference in longitudinal strain shows monotonic evolution between the two limiting values defined by relation (75). The variation is controlled by parameter λ_τ as predicted by relations (72) and (73). The normalised strain remains constant during crack propagation when observed above cracked region. Notwithstanding, due to imperfect boundary conditions, and adhesive failure, a crack closure compressive stress is observed at the crack tip whose amplitude decreases during propagation. This evolution is more complex to investigate, but is very similar to that observed in part II of this work. Soft contact, and a gap between spacer and adherend explain the development of crack closure compressive stress at the crack tip which may delay crack onset. A rapid strain variation is also observed at the transition between bonded and cracked regions due to strain accommodation, as explained in Section 5.2. From the stress values, the stress ratio τ/σ is computed. A significant compressive stress is observed with short cracks ($a < 0.3.L$), for which unstable propagation is generally observed. It is therefore suggested that longer starting cracks be used to perform such experiments but also that friction effect should be investigated for better understanding of this experiment.

6. Concluding remarks for the instrumented ENF test

The End Notched Flexure (ENF) test is among the most widely used techniques to study mode II fracture. However, the test suffers from a limited number of reliable and precise data about crack propagation and process zone phenomena. In general, applied force and resulting displacement diagrams are presented and investigated. This, we believe, cannot be regarded as sufficient for verification and validation of complex analytical or numerical models. In this contribution, we have developed a phenomenological description of the ENF test using a Timoshenko beam on a two-parameters elastic foundation model. With this we aim to compare findings with the data as evaluated with strain gauge instrumentation. Such a comparison is valid provided linear elastic behaviour is a reasonable approximation. Further work on strong non-linearity will be considered in the near future to extend the proposed technique to the characterisation of an elastoplastic interface with or without damage. Here, general remarks concerning preparation and conduction of the instrumented ENF test are given, which are relevant for the bonded system studied in the second part of this project. The importance of boundary conditions and the effect of adhesive, rather than cohesive failure are outlined.

During the ENF experiment, applied force and resulting deflection are measured. From these data, apparent instantaneous, crack position can be estimated using relation (78). This apparent value is bigger than the geometrical/real one, but evolution with time is expected to be monotonic. With simple beam theory, longitudinal skin strain along the debonded and bonded zones can be approximated with relation (75), used here for normalisation. The progression between these two values is mostly controlled by parameter λ_τ according to the relation (73), obtained with the simplified model. This approximation is valid provided the crack length is within the interval $\approx L/3 < a < \approx L - 1/\lambda_\tau$. Due to asymmetric loading conditions, a small crack closure effect due to compressive stress at the crack tip is to be expected. This will decrease with crack growth. To separate symmetric (crack closure) and antisymmetric mode II contributions, two strain gauges should be bonded at the same position along the span, one being bonded to the upper side, the other on the lower side. The difference between these two signals leads to the mode II contribution and their addition allows to evidence crack closure effect.

Application of this method will be presented in detail in the second part of this work.

Annexe

To obtain relations (34)–(39), we use the following integration procedure. First, we replace $\sigma(x)$ in Eq. (15) by expression (26). Integrating over x leads to:

$$T^i(x) = s\sum_{k=1}^{4} w\frac{F_k}{\lambda_k} exp(\lambda_k x) + A_i \tag{34}$$

Replacing $T^i(x)$ by expression (34) and $\tau(x)$ by expression (27) in relation (14), and integrating over x, we find:

$$M^i(x) = -s\sum_{k=1}^{4} w\frac{F_k}{\lambda_k^2} exp(\lambda_k x) + \frac{t}{2}\sum_{k=5}^{6} w\frac{F_k}{\lambda_k} exp(\lambda_k x) + \left(\frac{t}{2} w\tau_m - A_i\right)x + B_i \tag{35}$$

Finally from relation (17) and (18), the beam rotation φ^i and deflection v^i are found:

$$\varphi^i(x) = \frac{1}{EI}\left\{-s\sum_{k=1}^{4} w\frac{F_k}{\lambda_k^3} exp(\lambda_k x) + \frac{t}{2}\sum_{k=5}^{6} w\frac{F_k}{\lambda_k^2} exp(\lambda_k x) + \frac{1}{2}\left(\frac{t}{2} w\tau_m - A_i\right)x^2 + B_i x\right\} + C_i \tag{36}$$

$$v^i(x) = \frac{1}{EI}\left\{-s\sum_{k=1}^{4} w\frac{F_k}{\lambda_k^4} exp(\lambda_k x) + \frac{t}{2}\sum_{k=5}^{6} w\frac{F_k}{\lambda_k^3} exp(\lambda_k x) + \frac{1}{6}\left(\frac{t}{2} w\tau_m - A_i\right)x^3 + \frac{1}{2}B_i x^2\right\} + \left(C_i + \frac{A_i}{\kappa GS}\right)x + D_i + \frac{s}{\kappa GS}\sum_{k=1}^{4} w\frac{F_k}{\lambda_k^2} exp(\lambda_k x) \tag{37}$$

Similarly, replacing $\tau(x)$ with expression (27) in relation (16) and integrating over (16) we find:

$$N^i(x) = s\left[w\tau_m x + \sum_{k=5}^{6} w\frac{F_k}{\lambda_k} exp(\lambda_k x)\right] + E^i \tag{38}$$

Finally, integrating relation (19) we obtain:

$$u^i(x) = \frac{1}{ES}\left[s\left(w\tau_m\frac{x^2}{2} + \sum_{k=5}^{6} w\frac{F_k}{\lambda_k^2} exp(\lambda_k x)\right) + E^i x\right] + G^i \tag{39}$$

References

Adams, R.D., Peppiatt, N.A., 1974. Stress analysis of adhesive-bonded lap-joints. J. Strain Anal. Eng. Des. 9, 185–196.

Alfano, G., 2006. On the influence of the shape of the interface law on the application of cohesive-zone models. Comp. Sci. Technol. 66, 723–730.

Alfredsson, K.S., 2004. On the instantaneous energy release rate of the end-notch flexure adhesive joint specimen. Int. J. Solids Struct. 41, 4787–4807.

Arrese, A., Mujika, F., 2008. Influence of bending rotations on three and four-point bend end notched flexure tests. Eng. Fract. Mech. 75 (14), 4234–4246.

Arrese, A., Carbajal, N., Vargas, G., Mujika, F., 2010. A new method for determining mode II R-curve by the end-notched flexure test. Eng. Fract. Mech. 77, 51–70.

Barrett, J.D., Foschi, R.O., 1977. Mode II stress-intensity factors for cracked wood beams. Eng. Fract. Mech. 9 (2), 371–378.

Bennati, S., Colleluori, M., Corigliano, D., Valvo, P.S., 2009. An enhanced beam-theory model of the asymmetric double cantilever beam (ADCB) test for composite laminates. Comp. Sci. Technol. 69, 1735–1745.

Bennati, S., Taglialegne, L., Valvo, P.S., 2010. Modelling of interfacial fracture of layered structures. In: ECF 18–18th European Conference on Fracture, Fracture of Materials and Structures from Micro to Macro Scale, Dresden, Germany, August 30–September 3.

Ben Salem, N., Budzik, M.K., Jumel, J., Shanahan, M.E.R., Lavelle, F., 2012. Data reduction method and experimental set-up to study crack front mechanical fields in the double cantilever beam adhesion test. Eng. Fract. Mech., under review.

Blackman, B.R.K., Kinloch, A.J., Paraschi, M., 2005. The determination of the mode II adhesive fracture resistance, G_{IIC}, of structural adhesive joints: an effective crack length approach. Eng. Fract. Mech. 72 (6), 877–897.
Budzik, M.K., Jumel, J., Shanahan, M.E.R., 2011a. An in situ technique for the assessment of adhesive properties of a joint under load. Int. J. Fract. 171 (2), 111–124.
Budzik, M.K., Jumel, J., Shanahan, M.E.R., 2011b. Process zone in the single cantilever beam under transverse loading – Part II Experimental. Theor. Appl. Fract. Mech. 56, 13–21.
Carlsson, L.A., Gillespie Jr, J.W., Pipes, R.B., 1986. On the analysis and design of end notched flexure (ENF) for mode II testing. J. Compos. Mater. 20, 594–604.
Chai, H., Mall, S., 1988. Design aspects of the end-notch adhesive joint specimen. Int. J. Fract. 36 (1), 3–8.
Chai, H., 1992. Micromechanics of shear deformations in cracked bonded joints. Int. J. Fract. 58 (3), 223–239.
Cognard, J.Y., Davies, P., Sohier, L., Créac'hcadec, R., 2006. A study of the non-linear behaviour of adhesively-bonded composite assemblies. Compos. Struct. 76 (1–2), 34–46.
Cognard, J.Y., Sohier, L., Davies, P., 2011. A modified Arcan test to analyze the behavior of composites and their assemblies under out-of-plane loadings. Compos. Part A – Appl. S. 42 (1), 111–121.
Corleto, C.R., Hogan, H.A., 1995. Energy-release rates for the ENF specimens using a beam on an elastic foundation. J. Compos. Mat. 29 (11), 1420–1436.
Ding, W., Kortschot, M.T., 1999. A Simplified beam analysis of the end notched flexure mode II delamination specimen. Compos. Struct. 45 (4), 271–278.
Duarte, A.P., Coelho, J.F., Bordalo, J.C., Cidade, M.T., Gil, M.H., 2011. Surgical adhesive: Systematic review of the main types and development forecast. Prog. Polym. Sci. 37 (8), 1031–1050.
Goglio, L., Rossetto, M., 2011. Precision of the one-dimensional solutions for bonded double lap joints. Int. J. Adhes. Adhes. 31 (5), 301–314.
Goland, M., Buffalo, N.Y., Reissner, E., 1944. The stresses in cemented joints. J. Appl. Mech. – T. ASME 11, 17–27.
Griffith, A.A., 1921. The phenomena of rupture and flow in solids. Philos. Trans. Roy. Soc. Lond. Ser. A 221, 163–198.
Gustafson, P.A., Waas, A.M., 2009. The influence of adhesive constitutive parameters in cohesive zone finite element models of adhesively bonded joints. Int. J. Solids Stucts. 46, 2201–2215.
He, X., 2011. A review of finite element analysis of adhesively bonded joints. Int. J. Adhes. Adhes. 31 (4), 248–264.
Higgins, A., 2000. Adhesive bonding of aircraft structures. Int. J. Adhes. Adhes. 20, 367–376.
Li, Y., Wong, C.P., 2006. Recent advances of conductive adhesives as a lead-free alternative in electronic packaging: materials, processing, reliability and applications. Mater. Sci. Eng. 51 (1–3), 1–35.
Liljedahl, C.D.M., Crocombe, A.D., Wahab, M.A., Ashcroft, I.A., 2007. Modelling the environmental degradation of adhesively bonded aluminium and composite joints using a CZM approach. Int. J. Adhes. Adhes. 27 (6), 505–518.
Loven, W.E., 1999. Structural bonding of composites in the transportation market. Reinforced Plastics 43 (6), 40–43.
Lundsgaard-Larsen, C., Sørensen, B.F., Berggreen, C., Ostergaard, R.C., 2008. A modified DCB sandwich specimen for measuring mixed-mode cohesive laws. Eng. Fract. Mech. 75 (8), 2514–2530.
Luo, Q., Tong, L., 2009. Analytical solutions for non-linear analysis of composite single-lap adhesive joints. Int. J. Adhes. Adhes. 29 (2), 144–154.
Van Meerbeek, B., Perdigao, J., Lambrechts, P., Vanherle, G., 1998. The clinical performances of adhesives. J. Dent. 26 (1), 1–20.
de Moura, M.F.S.F., de Morais, A.B., 2008. Equivalent crack based analyses of ENF and ELS tests. Eng. Fract. Mech. 75, 2584–2596.
de Moura, M.F.S.F., Silva, M.A.L., de Morais, A.B., Morais, J.J.L., 2006. Equivalent crack based mode II fracture characterization of wood. Eng. Fract. Mech. 73, 978–993.
Murthy, M.V.V.S., Roy Mahapatra, D., Badarinarayana, K., Gopalakrishnan, S., 2005. A refined higher order finite element for asymmetric composite beams. Comp. Struct. 67, 27–35.
Oehlers, D.J., 2001. Development of design rules for retrofitting by adhesive bonding or bolting either FRP or steel plates to RC beams or slabs in bridges and buildings. Compos. Part A – Appl. S. 32, 1345–1355.
Ouyang, Z., Li, G., 2009. Nonlinear interface shear fracture of end notched flexure specimens. Int. J. Solids Struct. 46, 2659–2668.
Qiao, P., Wang, J., 2005. Novel Joint deformation models and their application to delamination fracture analysis. Compos. Sci. Technol. 65, 1826–1839.
Raghu Prasad, B.K., Pavan Kumar, D.V.T.G., 2008. Analysis of composite ENF specimen using higher order beam theories. Thin Wall Struct. 46, 676–688.
Reddy, J.N., Wang, C.M., Lee, K.H., 1997. Relationships between bending solutions of classical and shear deformation beam theories. Int. J. Solids Struct. 34 (26), 3373–3384.
Roark, R.J., Young, W.C., Budynas, R.G., 2002. Roark's Formulas for stress and strain, 7th ed. Mc Graw-Hill, New-York.
Rodríguez, R.Q., Portilho de Paiva, W., Sollero, P., Rodrigues, M.R.B., Lima de Albuquerque, É., 2012. Failure criteria for adhesively bonded joints. Int. J. Adhes. Adhes. 37, 26–36.
Russel, A.J., Street, K.N., 1982. Factors affecting the interlaminar fracture energy of graphite/epoxy laminates. Progress in science and engineering of composites. In: Proceedings of ICCM-IV, Tokyo, 279-86.
Shokrieh, M.M., Heidari-Rarani, M., Ayatollahi, M.R., 2011. Calculation of GI for a multidirectional composite double cantilever beam on two-parametric elastic foundation. Aerosp. Sci. Technol. 15 (7), 534–543.
Shokrieh, M.M., Heidari-Rarani, M., Ayatollahi, M.R., 2012. Interlaminar fracture toughness of unidirectional DCB specimens: a novel theoretical approach. Polym. Test. 31, 68–75.
da Silva, L.F.M., das Neves, P.J.C., Adams, R.D., Spelt, J.K., 2009. Analytical models of adhesively bonded joints—Part I: Literature survey, Int. J. Adhes. Adhes., 29(3), 319-330.
Sørensen, B.F., Jacobsen, T.K., 2009. Characterizing delamination of fibre composites by mixed mode cohesive laws. Compos. Sci. Technol. 69, 445–456.
Sørensen, B.F., Jacobsen, T.K., 2003. Determination of cohesive laws by the *J* integral approach. Eng. Fract. Mech. 70, 1841–1858.
Sun, X., Davidson, B.D., 2006. Numerical evaluation of the effects of friction and geometric nonlinearities on the energy release rate in three- and four-point bend end-notched flexure tests. Eng. Fract. Mech. 73, 1343–1361.
Tanaka, H., Kageyama, K., Hojo, M., 1995. Prestandardization study on mode II interlaminar fracture toughness test for CFPR in Japan. Composites 26, 257–267.
Timoshenko, S.P., 1921. On the correction for shear of the differential equation for transverse vibrations of prismatic bars. Philos. Mag. 41, 744–746.
Volkersen, O., 1938. Die Nietkraftverteilung in zugbeanspruchten Nietverbindungen mit konstanten Laschenquerschnitten. Luftfahrtforschung 15, 41–47.
Wang, J., Qiao, P., 2005. Analysis of beam-type fracture specimens with crack-tip deformation. Int. J. Fract. 123, 223–248.
Yang, Q.D., Thouless, M.D., Ward, S.M., 2001. Elastic–Plastic mode-II fracture of adhesive joints. Int. J. Solids Struct. 38, 3251–3262.
Yoshihara, H., 2005. Mode II initiation fracture toughness analysis for wood obtained by 3-ENF test. Compos. Sci. Technol. 65, 2198–2207.
Yoshihara, H., 2010. Mode I and mode II initiation fracture toughness and resistance curve of medium density fiberboard measured by double cantilever beam and three-point bend end-notched flexure tests. Eng. Fract. Mech. 77, 2537–2549.
Zhao, B., Lu, Z.H., Lu, Y.N., 2011. Closed-form solutions for elastic stress–strain analysis in unbalanced adhesive single-lap joints considering adherend deformations and bond thickness. Int. J. Adhes. Adhes. 31 (6), 434–445.